

## Remodeling of Endogenous Mammary Epithelium by Breast Cancer Stem Cells

NATESH PARASHURAMA,<sup>a†</sup> NEETHAN A. LOBO,<sup>b†</sup> KEN ITO,<sup>a</sup> ADRIANE R. MOSLEY,<sup>b</sup> FREZGHI G. HABTE,<sup>a</sup> MAIDER ZABALA,<sup>b</sup> BRYAN R. SMITH,<sup>a</sup> JESSICA LAM,<sup>b</sup> IRVING L. WEISSMAN,<sup>b,f</sup> MICHAEL F. CLARKE,<sup>b,e,h</sup> SANJIV S. GAMBHIR<sup>a,c,d,g</sup>

<sup>a</sup>Molecular Imaging Program @Stanford, Department of Radiology, Division of Nuclear Medicine, Stanford University School of Medicine, Stanford, CA, USA; <sup>b</sup>Institute for Stem Cell Biology and Regenerative Medicine, Stanford University School of Medicine, Stanford, CA, USA; <sup>c</sup>Canary Center for Early Detection of Cancer, Palo Alto, CA, USA; <sup>d</sup>Departments of Bioengineering, <sup>e</sup>Internal Medicine (Oncology), <sup>f</sup>Pathology, Stanford University School of Medicine Stanford, CA, USA; <sup>g</sup>Department of Materials Science and Engineering, Stanford University, Stanford, CA, USA; <sup>h</sup>Program in Cellular and Molecular Biology, Stanford University School of Medicine, Stanford, CA, USA

**Key Words.** Cancer stem cells • Intravital microscopy • Breast cancer • Molecular imaging • MMTV-Wnt1 • Mammary stem cells

### ABSTRACT

Poorly regulated tissue remodeling results in increased breast cancer risk, yet how breast cancer stem cells (CSC) participate in remodeling is unknown. We performed *in vivo* imaging of changes in fluorescent, endogenous duct architecture as a metric for remodeling. First, we quantitatively imaged physiologic remodeling of primary branches of the developing and regenerating mammary tree. To assess CSC-specific remodeling events, we isolated CSC from MMTV-Wnt1 (mouse mammary tumor virus long-term repeat enhancer driving Wnt1 oncogene) breast tumors, a well studied model in which tissue remodeling affects tumorigenesis. We confirm that CSC drive tumorigenesis, suggesting a link between CSC and remodeling. We find that normal, regenerating, and developing gland maintain a specific branching pattern. In contrast, transplanta-

tion of CSC results in changes in the branching patterns of endogenous ducts while non-CSC do not. Specifically, in the presence of CSC, we identified an increased number of branches, branch points, ducts which have greater than 40 branches (5/33 for CSC and 0/39 for non-CSC), and histological evidence of increased branching. Moreover, we demonstrate that only CSC implants invade into surrounding stroma with structures similar to developing mammary ducts (nine for CSC and one for non-CSC). Overall, we demonstrate a novel approach for imaging physiologic and pathological remodeling. Furthermore, we identify unique, CSC-specific, remodeling events. Our data suggest that CSC interact with the microenvironment differently than non-CSC, and that this could eventually be a therapeutic approach for targeting CSC. *STEM CELLS* 2012;30:2114–2127

Disclosure of potential conflicts of interest is found at the end of this article.

### INTRODUCTION

Remodeling is a general process during tissue homeostasis. The mammary gland is a unique model for remodeling because it regularly undergoes coordinated changes in ductal epithelium and surrounding stroma [1]. Physiological remodeling occurs during breast development, the reproductive cycle, parturition, postlactational involution, and age-based mammary gland regression [2]. Importantly, these physiologic stages of remodeling are correlated with an increased risk of breast cancer. For example, cancers between premenopausal

women and postmenopausal women differ in estrogen receptor status (ER<sup>+</sup>) or ER<sup>-</sup> as well as in their clinical stage of presentation [3]. Furthermore, enhanced premenopausal remodeling reduces breast cancer risk [4], and poor remodeling after pregnancy increases cancer risk [5]. Overall, improper remodeling enhances cancer risk, but specific mechanisms are difficult to determine in clinical models. Thus new approaches are needed to assess remodeling.

Remodeling during growth of the normal mammary tree may be related to remodeling during growth of a tumor. The normal murine mammary epithelium uses invasion of terminal end buds (TEB), ductal elongation, lateral (side) budding and branching as

<sup>†</sup>Contributed equally to this work.

Author contributions: N.P., N.A.L., M.F.C., and S.S.G.: conceived of, conceptualized, the study. N.P. and N.A.L.: designed the experiments. N.P. and N.A.L. performed *in vivo* experiments with help of J.L., A.R.M., M.Z., and K.I. N.P. and N.A.L. collected and assembled data, with help of K.I. and B.R.S.; N.P., N.L., and F.B.H.: performed data analysis and interpretation; S.S.G. and M.F.C.: provided financial support; N.P., N.A.L., S.S.G., and M.F.C.: wrote and revised the manuscript, with final approval by I.L.W., M.F.C., and S.S.G.

Correspondence: Sanjiv S. Gambhir, M.D., Ph.D., Molecular Imaging Program @Stanford, Department of Radiology, Division of Nuclear Medicine, James H. Clark Center, Stanford University, 318 Campus Drive, E153, Stanford, CA 94305, USA. Telephone: 650-725-2309; Fax: 650-724-4948; e-mail: sgambhir@stanford.edu Received January 30, 2012; accepted for publication July 3, 2012; first published online in *STEM CELLS EXPRESS* August 16, 2012. © AlphaMed Press 1066-5099/2012/\$30.00/0 doi: 10.1002/stem.1205

mechanisms of remodeling [6]. Importantly, physiologic remodeling is disrupted in murine cancer [6, 7]. In the MMTV-Wnt1 (Mouse Mammary Tumor Virus-Wnt1 Oncogene) breast cancer model, mice initially develop increased number of branched ducts, indicating abnormal remodeling [8]. Furthermore, studies of MMTV-Wnt1 breast cancer mice have demonstrated that major mediators of tumorigenesis also appear to be involved in remodeling; these include extracellular matrix modulators (Matrix Metalloproteinases (MMP)/Tissue Inhibitors of Matrix Metalloproteinases (TIMP) [9]), soluble peptide factors/coreceptors (Fgf8 [10], Lrp6 [11]), and cell surface proteins (Syndecan [12]). However, the sheer number of remodeling factors identified (over 50 molecules) suggests that new approaches are needed to collectively assess the effects of individual remodeling factors.

Data suggest that remodeling may be regulated not only by various molecular factors but also by specific cellular subsets of parenchymal tissue. For example, during remodeling, major changes occur in mammary epithelial mass. This suggests that mammary stem cells (MSC), a rare cellular subset which drives changes in epithelial mass, may also drive remodeling. Furthermore, MSC and their immediate progenitors Mammary Colony Forming Cells (MaCFC) have a role in ductal elongation [13, 14], and MSC are enriched in TEB [15]. By analogy, breast cancer has been shown to have tumorigenic or cancer stem cell subset (CSC) that drives tumor growth [16] in humans [17] and mice [18, 19]. In fact, CSC ( $\text{Lin}^- \text{Thy1}^+ \text{CD24}^+$ ) [18] that drive tumor growth and are radiation resistant [20] have been identified from MMTV-Wnt1 breast tumors. Given that normal mammary tree growth and tumor remodeling share similar molecular pathways, that MSC have an important role in normal remodeling, and that MSC and CSC share important properties [21, 22] CSC also might have a cell-specific role in pathological remodeling. However, virtually nothing is known about how CSC remodel tissue, and new approaches are needed for assessing remodeling by CSC.

Current techniques to evaluate ductal growth during remodeling involve histological and whole mount techniques. Histological techniques are limited to thin slices of tissue, which highlight tissue detail, while whole mount techniques highlight macroscopic ductal structures, and both are applied to excised, not intact tissues. A complementary approach is intravital imaging (IVM), which affords high sensitivity, multiplex capability, and high spatial resolution (less than  $1 \mu\text{m}$ ). IVM has been used to image the normal mammary gland [23], tumor-stromal interactions [24], and motile cells [25]. Other noninvasive techniques, such as MRI [26] and bioluminescence [27, 28], lack sensitivity and spatial resolution, respectively. In terms of tissue preparation, IVM using a tissue flap has certain advantages; it allows high-resolution images of native tissue and facilitates imaging of transplanted cells and fluorescent mammary ducts.

To understand how CSC remodel the mammary microenvironment, we developed a strategy based on transplantation of CSC with IVM of fluorescent, endogenous mammary glands. We imaged changes in *in vivo* endogenous duct structure as a metric of how specific cellular subsets remodel their microenvironment. We imaged the remodeling in response of cancer cell lines, non-CSC, or CSC. Only the CSC fraction remodeled the microenvironment with focal, dramatic changes in lateral budding and duct formation of host, endogenous mammary tree. We also observed that CSC, but not non-CSC, gave rise to ductal structures, similar to developing glands. Overall, we present a novel approach for assessing *in vivo* remodeling of tissue by cellular subsets of a primary tumor and identify CSC-specific remodeling events in living subjects.

## MATERIALS AND METHODS

### Transgenic Mice/Cell Line

The B6 pcx-GFP mouse [29], a kind gift from Dr. Yoshitake Nishimune, (Osaka, Japan), the B6.Cg-Tg CAG-DsRed\* MST1 Nagy/J mouse (#006051; Jackson Laboratory, Bar Harbor, ME, <http://www.jax.org>), the FvB CAG-GFP mouse (#003516; Jackson Laboratory), and the MMTV Wnt-1 FVB/NJ (#002934; Jackson Laboratory) were used in our studies. In all cases, GFP is used as an abbreviation for enhanced green fluorescent protein. These mice are described in the supporting information Methods section. The DB7 breast cancer cell line was previously derived from an FvB mammary tumor and is described in the supporting information section. It was a kind gift from Dr. Christopher Contag (Stanford, CA). All studies used only female mice.

### Molecular Imaging Agents/Dyes

A near-infrared imaging probe was used to image the microvasculature within the mammary fat pad (Angiosense-750; PerkinElmer, Waltham, MA, <http://www.perkinelmer.com>). Excitation was provided by the 748-nm infrared laser, and emission was captured using the Angiosense750 filter. A far-red dye (CellTrace Far Red ddAO-SE "(7-hydroxy-9H-(1,3-dichloro-9,9-dimethylacridin-2-one))", #C34553, Invitrogen, Carlsbad, CA, <http://www.invitrogen.com>) was used for cell labeling and is a long-term cell labeling dye which reacts with free amine groups on intracellular, cell surface, and extracellular proteins and other biomolecules. Excitation with ddAO was achieved with the 633-nm laser, and emission was captured with the Angiosense680 filter.

### Intravital Microscopy and Two-Photon Microscopy

All animal studies were approved by the Stanford Institutional Animal Care and Use Committee. For *in vivo* imaging, we used the miniature intravital laser scanning microscope optimized for *in vivo* imaging (Olympus IV 100, Olympus, Center Valley, PA). The system allows detection of four wavelengths, three of which can be acquired at the same time. Four lasers are used for excitation: (a) 488 nm air-cooled argon laser; (b) 561 nm solid-state laser; (c) 633-nm HeNe-R laser; (d) 748 nm infrared diode laser. The detection system consists of photomultiplier tubes that provide high quantum efficiency. Surgical procedure and imaging were performed on the microscope stage and a small animal volume-controlled respirator. FlouroView software (Version 1.7) was used to acquire all images. Imaging with two-photon microscopy is described in detail in the supporting information Methods and is performed only for images in supporting information Figure S3.

### Surgical Exposure of Tissue Flap Containing Mammary Gland

Surgery was performed on a covered, thin styrofoam board placed on a heated stage. The vertical and lateral portions of a Y-shaped incision used for clearing the fourth mammary fat pad were also used to expose the mammary gland for IVM [30]. The procedure was modified to allow imaging of the entire fourth mammary gland of the mouse. The details of this procedure are listed in supporting information Methods and are shown in supporting information Figure S1a–1c. Serial imaging in the flap involved making a new incision after 1 or 2 weeks, meticulous dissection, and imaging.

### Murine Mammary Stem Cell Isolation

Mammary glands from 6–12-week-old female C57BL/6J were dissociated as previously described [20] with minor modifications. Details are provided in supporting information Methods.

### Mammary Stem Cell Staining and Flow Cytometry

Staining and flow cytometry were performed as previously described [20]. Details of isolation provided in supporting information Methods.

### MMTV-Wnt1 Tumor Harvest and Dissociation

Briefly, tumors from MMTV-Wnt-1 FVB/NJ female transgenic mice were harvested and dissociated as described previously [18]. Briefly, tumors at 1–2 cm<sup>3</sup> (2–2.5 g) were isolated, minced, digested with a mixture of proteases (Blendzyme, Roche Diagnostics, Basel, Switzerland, <http://www.roche-applied-science.com>) for 2.5 hours at 38°C, filtered, exposed to ACK Lysis Buffer (GIBCO, Cat. #A10492-01) for red blood lysis, refiltered, suspended in staining medium, and stained using flow cytometry. For details, please see supporting information methods.

### MMTV-Wnt1 Cell Staining and Flow Cytometry

Briefly, cells were stained with Thy1.1-allophycocyanin, CD49f-fluorescein isothiocyanate, CD45-PE-Cy5, CD24, and 4',6-diamidino-2-phenylindole (DAPI), and then double sorted to ensure cell purity. The Lin<sup>-</sup> Thy1<sup>+</sup>CD24<sup>+</sup> cells were termed cancer stem cell (CSC) fraction, and the Non-Lin<sup>-</sup> Thy1<sup>+</sup>CD24<sup>+</sup> was termed non-cancer stem cell (non-CSC) fraction. For details, please see supporting information Methods.

### Cell Labeling and Normal MSC Transplants, CSC transplants, and DB7 Cell Transplants

For dye labeling of cells in Matrigel (Invitrogen), the cell solution was mixed with a 1:10 dilution of 20 μm (7-hydroxy-9H-(1,3-dichloro-9,9-dimethylacridin-2-one)) dye (#C34553, Invitrogen), stored on ice for at least 15 minutes, and then injected into the mammary fat pad. All injections were performed using a Hamilton Syringe (30 Gauge) using a cooled solution containing cells and Matrigel. For normal mammary

stem cell (MSC) studies, 50,000 Lin<sup>-</sup> cells were injected into donor mammary glands of 21-day-old female C57BL/6J mice, which had been cleared of endogenous mammary epithelium. For all cancer studies, cells were injected without clearing the fat pad first. For DB7 cell injections, 1,000 DB7 cells were mixed in a volume of 0.5 μl containing [1/2] Matrigel and [1/2] PBS and injected into 3-month-old virgin FvB-GFP mice. For DB7-GFP<sup>+</sup> cell injections, the same procedure was used as above, except that dye-labeled, DB7-GFP<sup>+</sup> cells were used and cells were injected into the BL6 CAG-dsRED mouse. For MMTV-Wnt1 tumor studies, Lin<sup>-</sup>Thy1<sup>+</sup>CD24<sup>+</sup> (CSC) and non-Lin<sup>-</sup>Thy1<sup>+</sup>CD24<sup>+</sup> (non-CSC) were used. For experiments testing effects of CSC on endogenous ducts, 2,500 CSC and non-CSC in a volume of 5 μl of Matrigel were injected into the fat pads of 3-week-old FvB-GFP mice. For experiments determining the imaging features of CSC, 10,000 CSC and non-CSC in a volume of 20 μl of Matrigel were dye labeled and injected into fat pad of 3-month-old virgin nude mice.

### Image Acquisition and Analysis

Acquisition of depth stack movies, motion correction, creation of maximum intensity projection images, calculation of fractional area, calculation of branching, and calculation of invasion imaging features are all detailed below. Depth stack movies were acquired with the ×4 objective, for which the field of view is 2,297.92 × 2,297.92 μm<sup>2</sup> or approximately 2.3 × 2.3 mm<sup>2</sup>. Each depth stack movie contains 40–100 slices at 5–20 μm per slice. Further details are in the supporting information Methods section.

### Motion Correction

Motion and uneven plane of imaging were two major problems with this approach, as can be seen in a typical movie (See supporting information Movies). To counteract these issues, motion correction was done using Image J (ImageJ v1.42q), using the Stackreg/Turboreg plugins. For creating a projection image from a depth stack, “Z stack” function was used, which generated a maximum intensity projection image. This maximum intensity projection image was used for further image analysis.

**Figure 1.** Serial *in vivo* imaging identifies major features of mammary tree and allows visualization of cell transplantation. (A): High magnification intravital image of normal mammary gland in a female, 3-month old, pax-GFP adult mouse. Bright green tube-like structures represent mammary glands. Labeled in top panel above are main structural features including end bud, mammary duct, and lateral bud. Bar = 250 μm. (B): Mosaic intravital images of normal mammary gland in a female, 3-month old, pax-GFP adult mouse. White frame denotes image in (A). Each individual image is projection image from a depth stack, and the mosaic is then constructed (see Materials and Methods). Bright green tube-like structures represent mammary glands. Bar = 500 μm. (C): Serial intravital imaging in the same mouse as (B), reopened after 2 weeks. The image is projection image from a depth stack (see Materials and Methods). Bright green tube-like structures represent mammary glands. End bud, mammary duct, and lateral bud. Bar = 500 μm. (D): Same image as in (C) except outlining of ducts performed on top of original image, followed by conversion to black and white (binary) image. Image is of repeat intravital imaging in the same mouse as (C), reopened after 2 weeks. The original image is projection image from a depth stack (see Materials and Methods). Bright green tube-like structures represent mammary glands. Bar = 500 μm. (E): Calculation of the duct area in normal and serially imaged female, 3-month old, pax-GFP mice from maximum intensity projection images. Average fractional area was quantified by outlining pax-GFP ducts as described in Materials and Methods. The fractional area for  $n = 3$  mice (three fields of view per mouse) are presented as the mean ± SD. (F): Triple branching mammary bud in female, 3-month old, pax-GFP mouse at high magnification (×10 objective). The image is projection image from a depth stack (see Materials and Methods). Arrow points to branching terminal end bud at high magnification. Bar = 100 μm. (G): Mammary duct and lumen in female, 3-month old, pax-GFP mouse at high magnification. The image is projection image from a depth stack (see Materials and Methods). Arrow (above) demonstrates ductal epithelium, a bilayer of epithelial cells surrounding lumen, and arrow (below) demonstrates duct lumen. Bar = 100 μm. (H): Composite, high magnification images taken immediately after transplantation of dye-labeled FvB-derived, DB7-GFP cells into female, 3-month-old, BL6 DsRED mammary gland. The image is projection image from a depth stack (see Materials and Methods). Background tissue appears red in DsRED mouse. Images acquired immediately after injection of 0.5 μl mixture of 1,000 DB7-GFP<sup>+</sup> cells and Matrigel. Bar = 100 μm. (I): Same as in (H) except, dye labeling (yellow channel) of the DB7-GFP cells is shown. Demonstrates visualization of dye labeled cells immediately after transplantation. Bar = 100 μm. (J): Composite, high magnification images taken 14 days after DB7-GFP<sup>+</sup> cell transplantation into female, 3-month old, BL6 DsRED mammary gland. The image is projection image from a depth stack (see Materials and Methods). Images acquired 14 days after injection of 0.5 μl mixture of 1,000 DB7-GFP<sup>+</sup> cells and Matrigel. Bar = 100 μm. (K): Same as in (H) except, dye labeling (yellow channel) of the DB7-GFP cells is shown. Demonstrates visualization of dye labeled cells 14 days after transplantation. Bar = 100 μm. Abbreviation: GFP, green fluorescent protein.

**Generation of Mosaic**

For generating a mosaic image, movies were acquired from overlapping fields of view, and a maximum projection image from each movie was generated. The presence of the mammary ducts was used for aligning of the projection images, which were “stitched” together using the “MosaicJ” plugin to

generate a single image which represents all the ducts from the entire fat pad.

**Fractional Area Calculation**

To calculate the average fractional area of mammary ducts, we analyzed the maximum intensity projection, motion

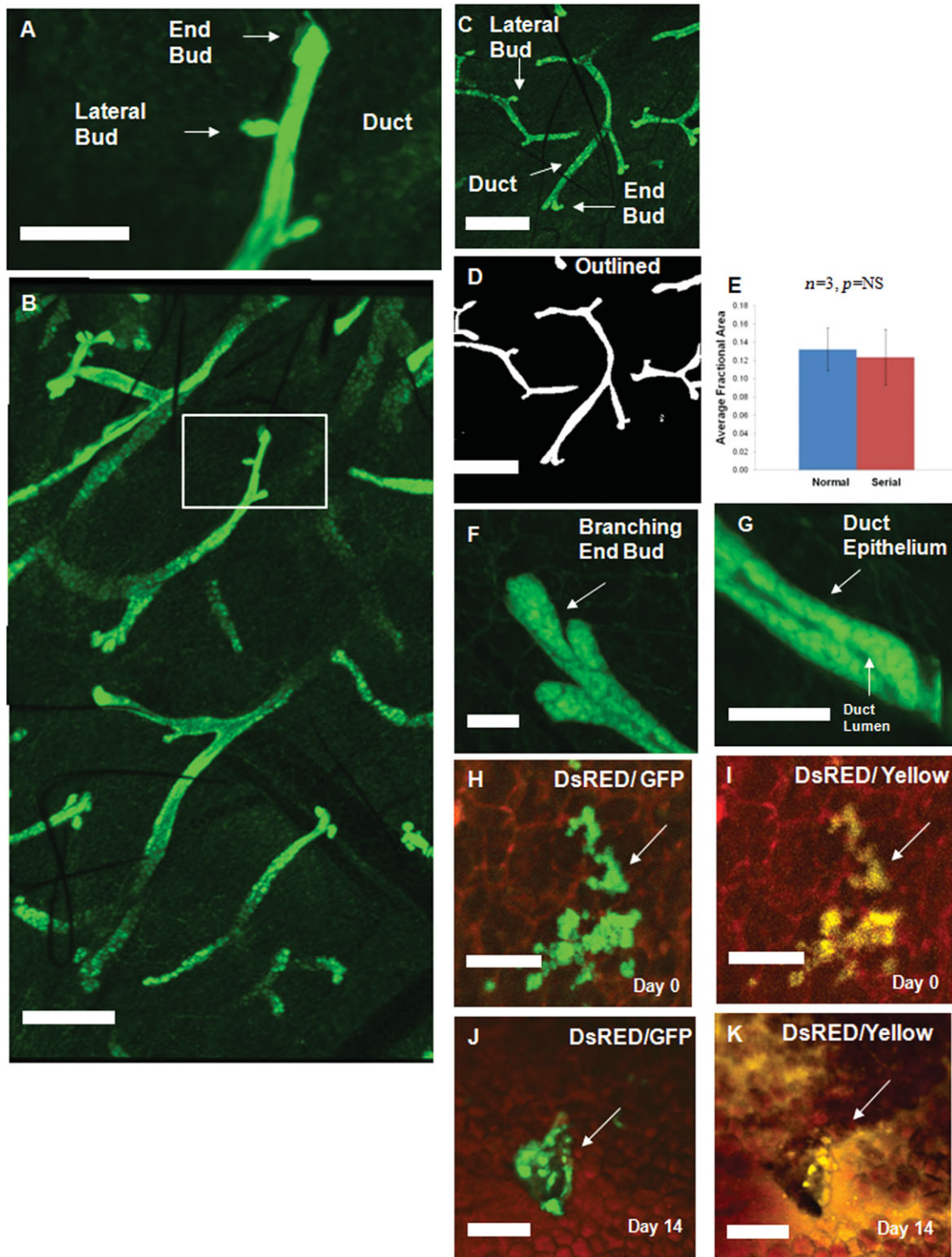


Figure 1

corrected live images of mammary ducts. We first outlined regions of interest (ROIs) around mammary trees of at least three, low magnification, fields of view per mouse. These were outlined by visually inspecting and then manually tracing each duct, using image J. All analysis was performed by a single individual (N.P.), to reduce variation in measurements. We then used the “fill function” on Image J, to fill the enclosed outlines of the ducts. Each ductal element in each field of view was a unique ROI, and, normally, the number of ROIs was usually 3–10 per field of view. Next, we calculated the area (number of pixels) of each ROI, summed the area from each ROI in a specific field of view, and divided this number by the total area of the image. We then compared the average fractional area covered by green fluorescent mammary trees in adult mice in various experimental conditions.

### Analysis of Branching of Mammary Tree After MMTV-Wnt1 Injection into FvB Mice

To convert ductal structures to skeletons, ducts were outlined, filled, and the entire image was converted to a binary image. The image was then processed using the “Skeletonize” function in ImageJ, and the final skeletonized image in each field of view was analyzed by the “Analyze Skeleton” tool. This image identifies all ROIs and calculates several metrics, including number of junctions, number of junction voxels, number of branches, average branch length, and slab voxels.

For analysis, we chose three independent fields of view for each condition in each mouse. For each field of view, we only analyzed ductal elements that contained three or more branches. For each ductal element in each field of view, we used slab voxels as an estimate of the total length of that specific ductal element. We first normalized each calculated metric by the number of slab voxels. The rationale for the normalization is as follows. If a duct element A has five branches and is 10 units long, whereas another ductal element B has five branches but is 1 unit long, we normalized each element so that for A, we have 0.5 branches/unit length and for B we have 5 branches/unit length. After normalization of each ductal element, we averaged the normalized value (for example, number of branches) across each ductal element for each field of view in one mouse. Next, we calculated the mean and standard deviation of this same number across all mice, and this was the final form of the data.

### Calculation of “invasiveness” Imaging Feature (Area Divided by Perimeter)

We observed that CSC transplants developed complex morphological features, whereas non-CSC did not. To develop a metric for these observations, we first outlined each  $\times 4$  image. Next we calculated the area and perimeter for each image. Finally, we calculated the ratio of area to perimeter. Thus, more complex shapes result in an enlarged perimeter in relation to area, which decreases the ratio.

### Statistical Analysis

For all calculations, the mean was calculated for three fields of view per mouse, and mean was averaged and standard deviation was calculated across multiple mice for each data point. Student’s *t* test was used to calculate *p* values with  $\alpha = 0.05$  significance level, with assumptions of a two-tailed distribution, and two samples of equal variance for all calculations.

## RESULTS

### Serial *In Vivo* Imaging Identifies Major Features of Mammary Tree and Allows Visualization of Cell Transplantation

In order to image how cells induce an endogenous remodeling response, we first developed a novel *in vivo* imaging technique of the adult fluorescent mammary gland (supporting information Fig. S1a–c). We used an adult, green fluorescent mouse that constitutively expresses high levels of green fluorescent protein (GFP), particularly in the mammary epithelium [29]. Using IVM, we first visualized important features of the mammary tree, including ducts, lateral buds, and end buds (Fig. 1A, 1B; supporting information Videos S1, S2). We validated these findings in two other strains of mice where expression of the GFP or DsRED transgene is driven by the same promoter (supporting information Fig. S2a, S2b). We imaged the fluorescent mice using two-photon microscopy, which showed that fluorescence signal indeed emanates primarily from mammary epithelium (supporting information Fig. S3a, S3b). Repeat imaging after 2 weeks demonstrated no architectural changes in the mammary tree (Fig. 1C). To estimate the amount of density of mammary ducts present, we calculated the fractional area covered by the mammary ducts in each image (See supporting information methods). Mammary ducts are clearly present and easily outlined visually. An example of a serially imaged duct, and the same image with ducts outlined is shown (Fig. 1C, 1D). In this case, there are six ROIs in the field of view, and the fractional area is 0.083, or 8.3% of total area in the image. With regard to normal versus serially imaged mice, the average fractional area was not statistically significant between the two cases ( $n = 3$  mice, Fig. 1E). At higher magnifications, we visualized further details of mammary bud and duct structures (Fig. 1F, 1G; supporting information Video S3). We extended our technique to imaging of dye-labeled breast cancer cell lines (DB7 cell line) after cell transplantation [30]. GFP<sup>+</sup> DB7 cells transplanted in adult DsRED mice (for differentiation from the GFP<sup>+</sup> cells) were readily detectable (Fig. 1H), correlated strongly with dye labeling (Fig. 1I), and could be visualized 2 weeks later (Figs. 1J, 1K). Overall, we showed that we could comprehensively and serially image both the fluorescent mammary tree and transplanted cells.

### *In Vivo* Imaging Demonstrates Global Remodeling During Regeneration

To image physiological remodeling, we first focused on ductal growth during regeneration. The regeneration assay is well studied [30] but has not been imaged or analyzed using *in vivo* imaging. First, we performed “bulk” transplantation of mammary epithelial cells containing unsorted MSC. We transplanted GFP<sup>+</sup> Lin<sup>-</sup> mammary epithelial cells into cleared pads of 3 week hosts, as done previously [20]. To visualize branching of glands during regeneration, we visualized both injected cells and branching, regenerating ducts after injection (Fig. 2A) and after 6, 10, and 16 weeks (Fig. 2B–2D) (supporting information Video S4). Immediately after transplantation, we observed fluorescence from transplanted cells with no apparent architectural organization (Fig. 2A). At 6 weeks, we observe sparse ductal trees (Fig. 2B). At 10 weeks, we observe more dense glands, often with TEB (Fig. 2C, rows). At 16 weeks, we observe a fully formed mammary tree, here shown as a mosaic of several images but no detectable TEB (Fig. 2D, Arrows). We converted each image into a skeletonized image (Fig. 2E, top and bottom panels), which was then analyzed

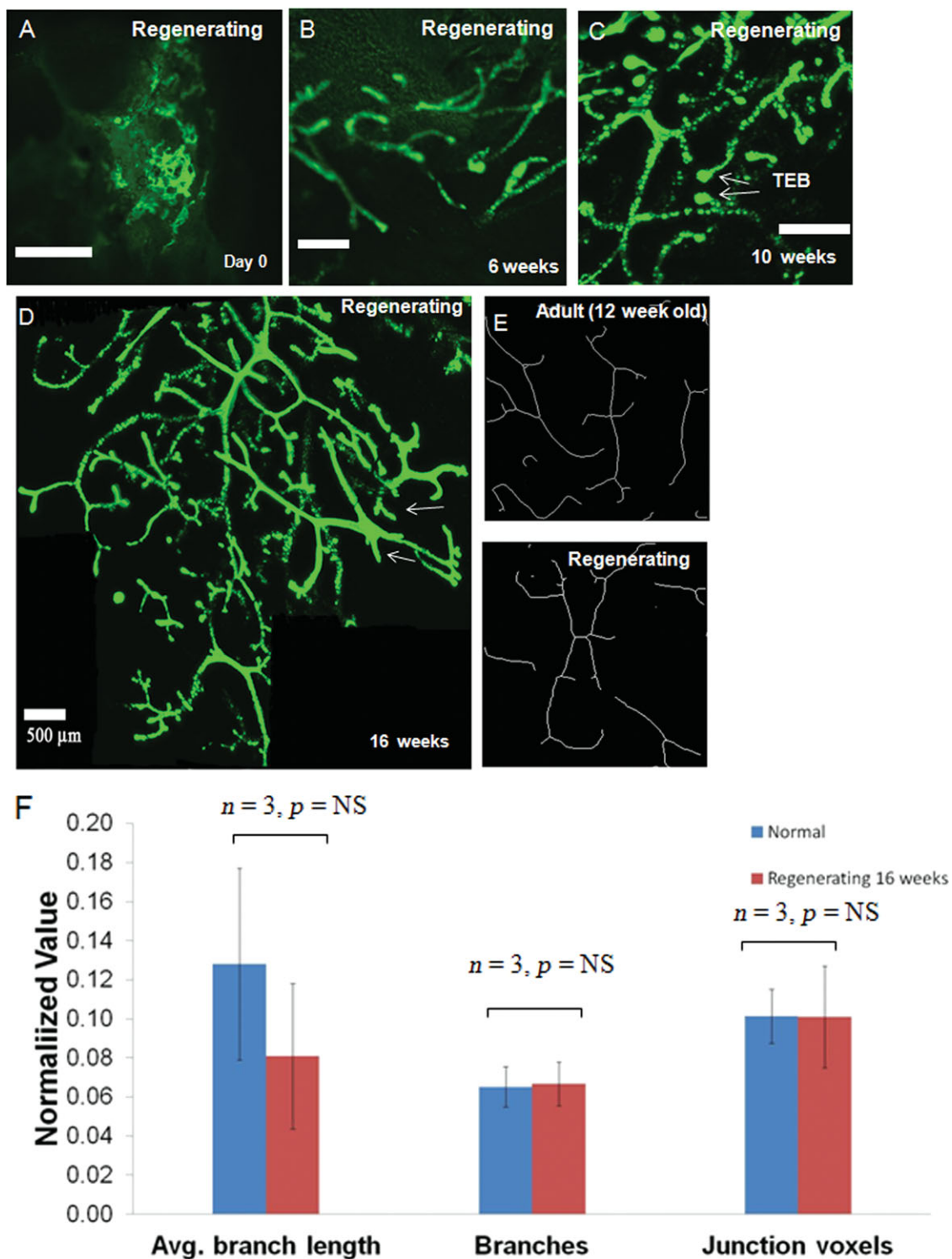


**Figure 2.** *In vivo* imaging demonstrates global remodeling during regeneration. (A): Imaging of Lin<sup>-</sup> GFP expressing mammary epithelial cells, immediately after transplantation into the cleared mammary fat pad of a wild-type BL6, female, 3-week-old mouse. Bar = 500  $\mu$ m. (B): Imaging of Lin<sup>-</sup> GFP expressing mammary epithelial cells, 6 weeks after transplantation into the cleared mammary fat pad of a wild-type BL6, female, 3-week-old mouse. Bar = 500  $\mu$ m. (C): Imaging of Lin<sup>-</sup> GFP expressing mammary epithelial cells, 10 weeks after transplantation into the cleared mammary fat pad of a wild-type, female, 3-week-old mouse. TEB are shown with arrows. Bar = 500  $\mu$ m. (D): Mosaic image of several images of Lin<sup>-</sup> GFP expressing mammary epithelial cells, 16 weeks after transplantation into the cleared mammary fat pad of a wild-type, female, 3-week-old mouse. The entire transplant is visualized. Bar = 500  $\mu$ m. (E): Skeletonized images of adult pax-GFP gland and regenerating gland, 16 weeks after transplantation demonstrating similar branching patterns. (F): Bar graph demonstrating average branch length, branches, and junction voxels per field of view per mouse for normal and regenerating (16 weeks after transplantation) mammary ducts. For each field of view, mammary ducts were outlined, skeletonized, and analyzed using an Image J Plugin (see Materials and Methods). Three fields of view per mouse, for  $n = 3$  mice, were analyzed, and data are presented as mean  $\pm$ SD. Abbreviations: GFP, green fluorescent protein; TEB, terminal end buds.

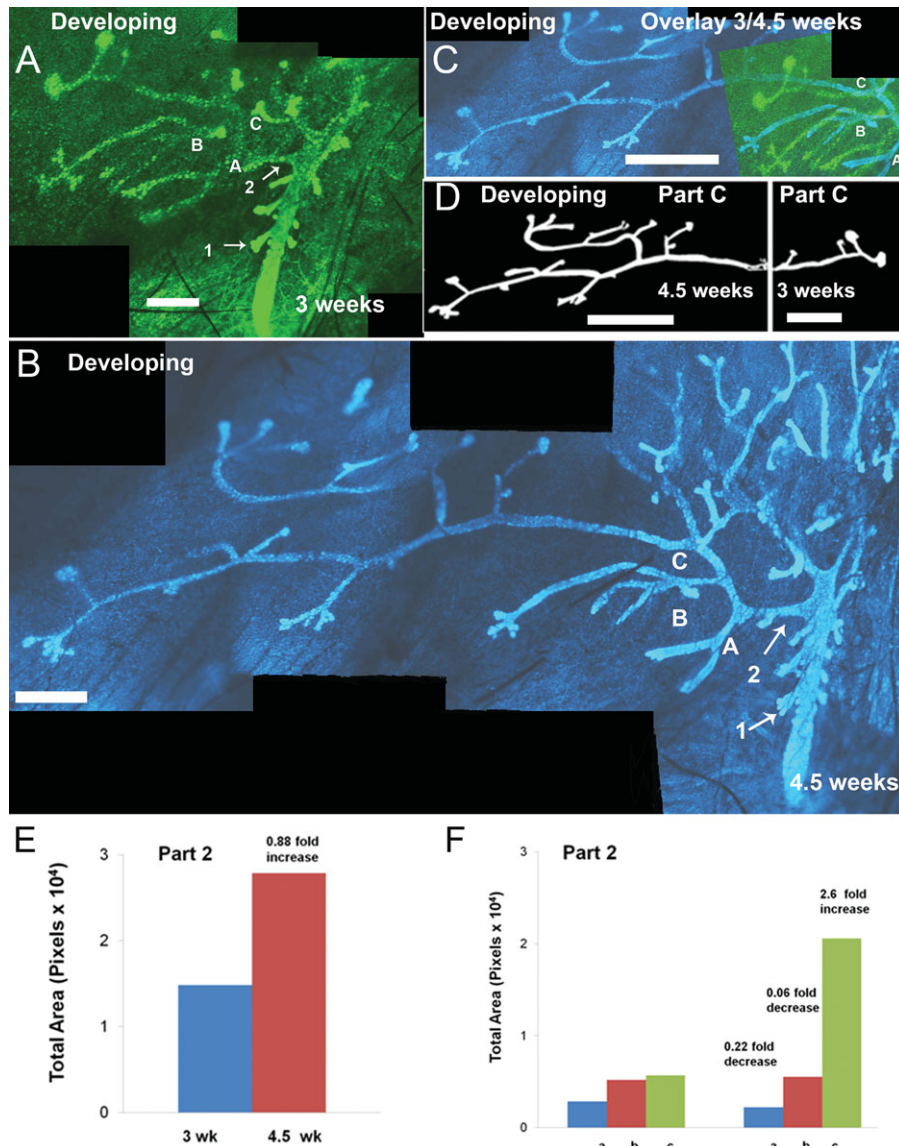


**Figure 3.** *In vivo* imaging demonstrates differential remodeling of individual ductal branches during mouse development. (A): Mosaic composed of several images taken of a developing female pax-GFP mouse at 3 weeks of age. Large green tubular structure in center extending vertically is primary mammary tree emanating from nipple. Secondary branches of mammary ducts are extending from mammary tree, to the left. Numbers 1 and 2 represent secondary branches (arrows) extending separately from tree and are separated by approximately 1,000  $\mu\text{m}$ . Branch 2 has separate branching parts labeled as A, B, and C. Black boxes are not part of primary image but are added to improve uniformity during figure assembly. Bar = 500  $\mu\text{m}$ . (B): Mosaic image of several projection images taken of the same developing female mouse as (A), at 4.5 weeks of age, recolored as blue for visual purposes only. Large blue tubular structure in center extending vertically is primary mammary tree emanating from nipple. Secondary branches of mammary ducts are extending from mammary tree, to the left. Numbers 1 and 2 represent secondary branches extending separately from tree and separated by approximately 1,000  $\mu\text{m}$ . Branch 2 has separate branching parts labeled as A, B, and C. Black boxes are not part of primary image but are added to improve uniformity during figure assembly. Bar = 500  $\mu\text{m}$ . (C): Overlay of branch two from mosaic images in (A) and (B). Branch 2 is overlaid demonstrating changes in branch growth, 10 days later. Images are overlaid by lining up primary mammary duct, which runs vertically in both images. Green fluorescent protein (GFP) (green) ducts are from 3 week time point, and blue (recolored from green for visual purposes) ducts are at the 4.5 weeks time point. Black boxes are not part of primary image but are added to improve uniformity during figure assembly. Bar = 500  $\mu\text{m}$ . (D): An outlined, binary image of branch 2, secondary branch C. Displayed in a “mirror” format with right side demonstrating branching pattern at 3 weeks, and left side at 4.5 weeks, and both at same scale. Both the 3 week and 4.5 week images have approximately three main branch points. Bar = 500  $\mu\text{m}$ . (E): Bar graph demonstrating quantitation of growth at 3 weeks and 4.5 weeks of branch 2. Total number of pixels was used as arbitrary units. Growth measurement was performed by outlining structures from same anatomical location in both images, and a 0.88-fold increase in overall growth was calculated. This was calculated by summing the growth of all components of part 2, including part A, B, and C. (F): Bar graph demonstrating quantitation of growth at 3 weeks and 4.5 weeks of branch 2. Data are comparison between components (A, B, and C) at 3 weeks to the same component in week 4.5. Total number of pixels was used as arbitrary units, and growth measurement was performed by outlining structures from same anatomical location in both images. Fold changes in growth for parts A, B, and C were 0.22-fold decrease, 0.06-fold decrease, and 2.6-fold increase, respectively.

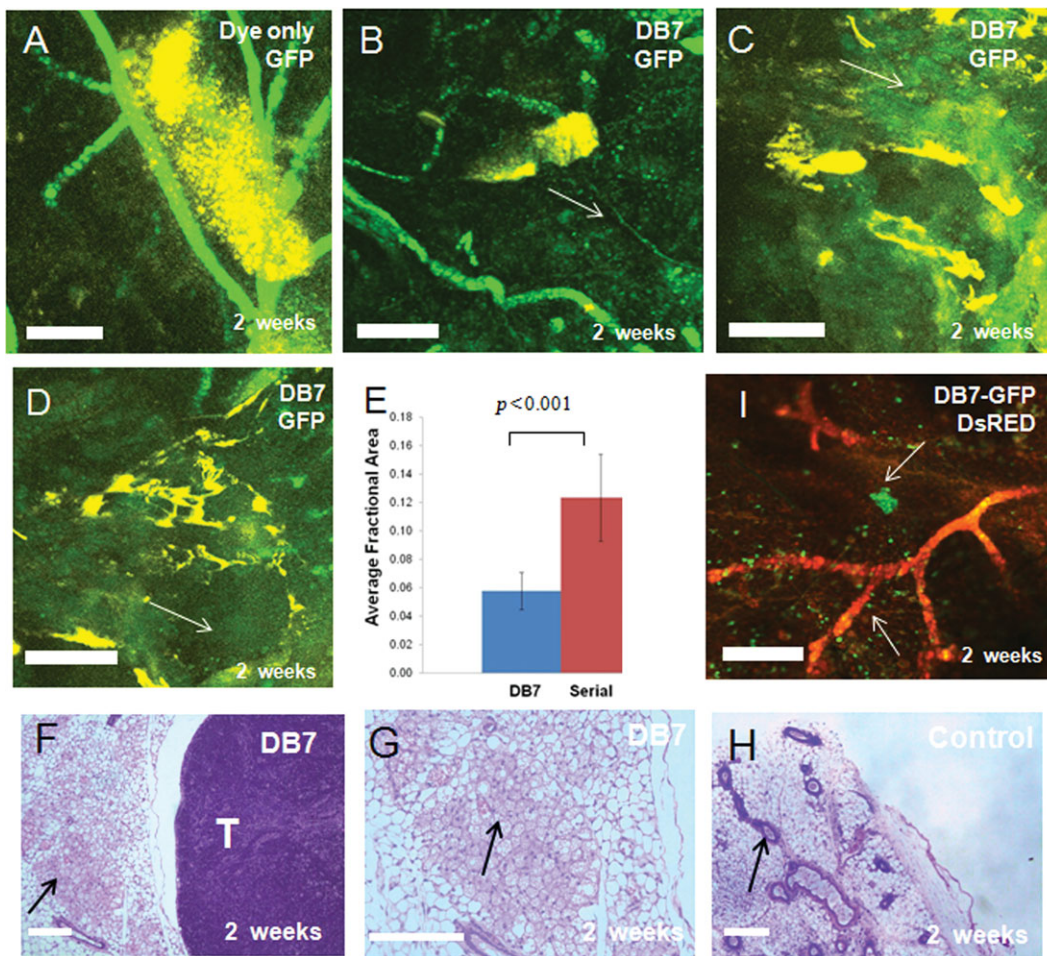


**Figure 4.** Transplantation of DB7 cells results in decreased duct signal from endogenous mammary tree. (A): Composite image of GFP (green) mammary ducts at the site of dye implantation (yellow) from female, 3-month old, FvB-GFP mouse. Normal ducts can be visualized, shown next to dye implant. Bar = 500  $\mu$ m. (B): Composite image of GFP (green) mammary ducts at the site of DB7 tumor implantation (yellow) from a female, 3-month old, FvB-GFP mouse. Bar = 500  $\mu$ m. Arrow demonstrates absence of ducts. (C): A second composite image of GFP (green) mammary ducts at the site of DB7 tumor implantation (yellow) from a female, 3-month old, FvB-GFP mouse. Bar = 500  $\mu$ m. Arrow demonstrates absence of ducts. (D): A third composite image of GFP (green) mammary ducts at the site of DB7 tumor implantation (yellow) from a female, 3-month old, FvB-GFP mouse. Bar = 500  $\mu$ m. Arrow demonstrates absence of ducts. (E): Bar graph demonstrating quantitation of fractional area of DB7 transplanted mammary glands and serially imaged mammary glands (control), 2 weeks after transplantation in female, 3-month old, FvB-GFP mice. Area was quantitated by outlining ducts as ROIs in at least three fields of view for  $n = 4$  mice for DB7 and  $n = 3$  mice for serial imaging, 2 weeks after implantation. Data are presented as mean  $\pm$  SD. (F): Image ( $\times 5$ ) of hematoxylin and eosin (H+E) stain of mammary gland 4 weeks after transplantation into female, 3-month old, FvB-GFP mice. Tumor edge designated by "T." Arrow designates stroma surrounding tumor edge. The lack of mammary ducts can be visualized on the tumor edge. Bar = 200  $\mu$ m. (G): High magnification image ( $\times 10$ ) of the same tissue in (A). Arrow designates lack of mammary ducts. Bar = 200  $\mu$ m. (H): Image ( $\times 5$ ) of hematoxylin and eosin (H+E) stain of normal mammary gland in 3-month old, FvB-GFP mice. Arrow designates normal mammary duct, of which several are present. Bar = 200  $\mu$ m. Abbreviation: GFP, green fluorescent protein.

quantitatively. We calculated the branch length, the number of branches and junction voxels for each ductal element (Fig. 2F). Importantly, we normalized each of these metrics by the length of the ductal element being analyzed. The total length of ductal elements did not differ between conditions, indicating each could be compared to the other (supporting information Fig. S4). Our analysis indicated that branching of regenerated ducts at 16 weeks, as measured by these metrics, was not statistically different than the normal mammary tree (Fig. 2F,  $n = 3$ ).

### ***In Vivo* Imaging Demonstrates Differential Remodeling of Individual Ductal Branches During Mouse Development**

As another model of remodeling, we examined the developing mammary gland using serial *in vivo* imaging. We performed imaging of the same mouse at 3 and 4.5 weeks of age and

arranged the images as a mosaic (Fig. 3A, 3B; supporting information Videos S5 [3 weeks] and S6 [4.5 weeks]). We repeated this procedure for several other mice ( $n = 3$  mice,  $n = 5$  mammary glands). Two advantages of this experimental system are the capability for serial imaging at large scales, or "whole" tissue imaging, and at the scale of an individual primary mammary duct. Image overlay between 3 and 4.5 weeks revealed that part C, primary branch 2, remodeled extensively through branching and elongation (Fig. 3C). To further visualize the differences in branch 2, part C at 3 and 4.5 weeks, we outlined the same duct at 3 and 4.5 weeks and placed them side-by-side (Fig. 3D). This demonstrated that three major branch points at 3 weeks on primary part C (right panel, Fig. 3D) can be also visualized at 4.5 weeks (left panel, Fig. 3D). To measure the increase in growth for branch 2, we calculated the area difference, and we observed an 88% increase in area from 3 to 4.5

weeks (Fig. 3E). Importantly, when we examine the data for each part of branch 2, we observe that branch 2, part C, grew 260%, while its neighbors A and B decreased in growth (Fig. 3F). To demonstrate that growth can be measured at higher magnification using serial imaging, we imaged branch 1 and demonstrated a 54% increase (supporting information Fig. S5a–S5c). Overall, we imaged individual remodeling events and observed asymmetric ductal growth during development.

### Transplantation of DB7 Cells Results in Decreased Duct Signal from Endogenous Mammary Tree

Before transplanting CSC, we wished to first establish the response of the endogenous tree to transplantation of a breast cancer cell line. We chose the DB7 cell line (derived from mutant MMTV-PyMT [Polyoma T Antigen]) mice [31, 32] because they have low metastatic potential, and therefore the cells should remain localized upon transplantation. We transplanted 1,000,

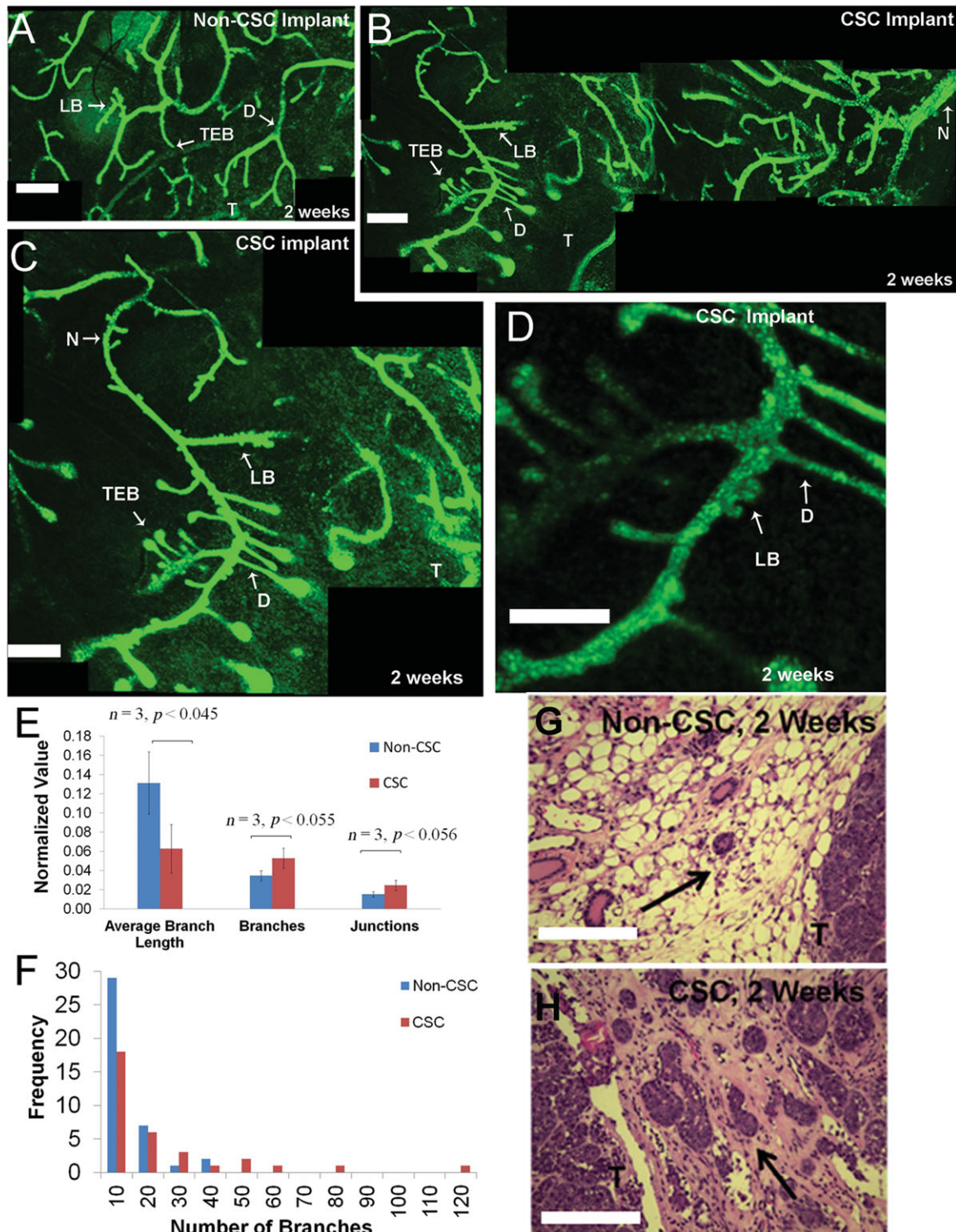


Figure 5.

dye-labeled DB7 cells into adult green fluorescent mice. We examined the remodeling response by determining changes in fractional area of endogenous ducts, in the same manner that we measured normal and regenerating glands. No changes were observed with injection of dye alone (Fig. 4A). However, we observed large regions with no detectable GFP signal in cases where dye staining was more focal (Fig. 4B). We also did not detect ducts in regions where dye staining was more punctuate and spread rather than focal (Fig. 4C, 4D). Analysis demonstrated a statistically significant decrease ( $p < .012$ ) in duct signal (Fig. 4E,  $n = 4$  mice). Supporting this data, histological sections demonstrated few, if any, ducts near the tumor border (Fig. 4F, 4G, black arrows) compared to normal duct (Fig. 4H). As a negative control, we changed the host to an allogeneic BL6-DsRED model (non-FvB background mouse), in which DB7-GFP cells appear to survive but not substantially replicate. As expected, we observed no changes to duct signal or architecture (Fig. 4I). Thus, the remodeling response of the DB7 breast cancer cell line was a reduction of endogenous duct signal but only when transplanted in syngeneic recipients.

### Transplantation of CSC from MMTV-Wnt1 Mice Results in Remodeling of Endogenous Mammary Tree

Next we hypothesized that CSC also remodel endogenous mammary tree as assessed by *in vivo* imaging. We initially isolated the CSC (Thy1<sup>+</sup>CD24<sup>+</sup>) or non-CSC (non-Thy1<sup>+</sup>CD24<sup>+</sup>) cells from a MMTV-Wnt1 tumor and tested for tumorigenicity. We injected 1,000 cells directly into the open mammary gland and observed that 5/5 tumors grew with transplanted CSC, whereas only 1/5 tumor grew with non-CSC. These data were consistent with tumorigenicity studies using the same cell surface markers from the MMTV-Wnt1 tumor model [18]. Next, we transplanted 2,500 CSC or non-CSC cells (to ensure more CSC are present) from MMTV-Wnt1 mammary tumors into the mammary fat pads of 3-week-old green fluorescent mice. To assess the remodeling response of the DB7 cells, we reimaged near the cell injection site after 2 weeks. Near the non-CSC tumors, we observed normal mammary gland architecture, with lateral buds (LB), TEB, and normal duct branching (D) near the tumor site (T) (Fig. 5A; supporting information Video S7,  $n = 3$  mice). Strikingly, near the CSC tumor site (T), we observed highly focal, increased LB, increased duct density (D), and enlarged end buds (TEB) (Fig. 5B; supporting information Video S8,  $n = 3$  mice). We observed these changes within the

normal mammary tree (Fig. 5C, top arrow “N”) and validated them at higher magnifications (Fig. 5C, 5D). We also observed the same changes in other mice, shown as single images (supporting information Fig. S6a, S6b), and in mosaic formats (supporting information Fig. S7). For quantitative assessment, we again analyzed branching patterns (supporting information Fig. S8a, S8b). To ensure proper analysis, we compared the total length of the ducts measured for CSC and non-CSC across each mouse. As expected, there was no difference in the total length of ducts measured per mouse for each condition (supporting information Fig. S8c). We analyzed each ductal element for branch length, number of branches, and number of junctions. Since some ductal elements were short and others were longer, we normalized all metrics for each ductal element by the length of the ductal element. CSC remodeling resulted in a statistically significant amount of shorter branches ( $p < .045$ ). Furthermore, we approached statistical significance for differences in number of branches ( $p < .055$ ) and number of branch points or junctions ( $p < .056$ ) (Fig. 5E, 5F,  $n = 3$  mice). We performed histogram analysis of the number of branches for all mice, and there were 0/39 elements with more than 40 branches for the non-CSC tumors, whereas there were 5/33 elements with 40 branches for the CSC tumors (Fig. 3G,  $n = 3$  mice). To further support our findings, we performed histological analysis. Overall microscopic tumor growth was similar at 2 weeks in both CSC and non-CSC (supporting information Fig. S8d, left and right panels, “T” for Tumor). Furthermore, increased ducts near the tumor border (T) in the CSC transplants were present compared to the non-CSC transplants (Fig. 5G [non-CSC], Fig. 5H [CSC]), consistent with *in vivo* images. We also observed extensive eosinophilic changes adjacent to the stroma of only CSC transplanted tumors (Fig. 5H, arrows).

We wanted to compare the phenotypes of the DB7 cell line and CSCs which have opposing effects on endogenous ducts. To accomplish this, we analyzed the MMTV-Wnt1 population and DB7 cells for the (Lin<sup>-</sup> Thy1<sup>+</sup> CD24<sup>+</sup>) and the (Lin<sup>-</sup> “Not Thy1<sup>+</sup> CD24<sup>+</sup>”) population. A flow cytometry plot for the MMTV-Wnt1 tumor-derived cells demonstrates that 0.7% of the cells are considered the CSC and the rest are considered the non-CSC (supporting information Fig. S9 left panel [top right gate] and right panel). Normally, the CSC are re-sorted a second time and repopulate the same gate (P5 population), which ensures purity. Analysis of the DB7 cell population demonstrated that approximately 13.2% of the cells appeared to have the same profile as the CSC (supporting information Fig. S10a left panel (top right gate) and right

**Figure 5.** Transplantation of CSC from MMTV-Wnt1 mice results in remodeling of endogenous mammary tree. (A): Mosaic, *in vivo* image of endogenous fluorescent mammary gland in female, 5-week-old FvB-GFP mouse, 2 weeks after transplantation of 2,500 non-CSC (non-Thy1<sup>+</sup>CD24<sup>+</sup>) cells. Site of tumor implantation is labeled at bottom of image (T). TEB and ducts (D) appear normal. A very small amount of LB is present in one of the mammary trees. Black boxes are not part of primary image but are added to improve uniformity during figure assembly. Bar = 500  $\mu$ m. (B): Mosaic, *in vivo* image of endogenous, fluorescent mammary gland in female, 5-week-old FvB-GFP mouse, 2 weeks after transplantation of 2,500 CSC (Thy1<sup>+</sup>CD24<sup>+</sup>) cells. Site of tumor implantation is labeled at bottom of image (T). Tumor site (T) is at bottom of image. Images taken across the entire mammary gland from nipple (N) throughout mammary gland. Changes in duct pattern noted with the presence of new LB, ducts (D), and TEB on left part of mosaic. Black boxes are not part of primary image but are added to improve uniformity during figure assembly. Bar = 500  $\mu$ m. (C): Same as (B) except focused mosaic image of altered ductal branching pattern. Tumor site (T) is at bottom right of image. Changes in duct pattern noted with the presence of new LB, ducts (D), and TEB. Ducts appear normal (N) at top of image, away from tumor. (T) Bar = 500  $\mu$ m. (D): Same as (C) except higher magnification view of altered ductal branching pattern. Tumor site is at bottom of image, out of view. Changes in duct pattern present with the presence of new LB, and Ducts (D). Bar = 200  $\mu$ m. (E): Bar graph demonstrating average branch length, number of branches, and number of junctions per field of view per mouse, for host mammary ducts in both the CSC and non-CSC transplantation experiments. For each field of view, mammary ducts were outlined, skeletonized, and analyzed using an Image J (see Materials and Methods). Three fields of view per mouse for  $n = 3$  mice, and data are presented as mean  $\pm$ SD. (F): Frequency histogram demonstrating same data in (E). Frequency histogram demonstrates the frequency of branches for each element that is calculated for both conditions, across all mice ( $n = 3$ ). Total of 33 ductal elements for CSC and 39 elements for non-CSC condition were analyzed. The CSC elements (red) have a few elements with a much larger number of branches. (G): Hematoxylin and Eosin (H+E) stain of mammary gland in non-CSC, 2 weeks after transplantation into 3-week-old FvB-GFP mice. Tumor edge designated by “T.” Arrow designates stroma surrounding tumor edge. The number of ducts can be visualized on the tumor edge. Stroma surrounding CSC contains many more ductal elements. (H): Same as above except in CSC condition. Abbreviations: CSC, cancer stem cell; D, duct; LB, lateral budding; T, tumor site; TEB, terminal end bud.

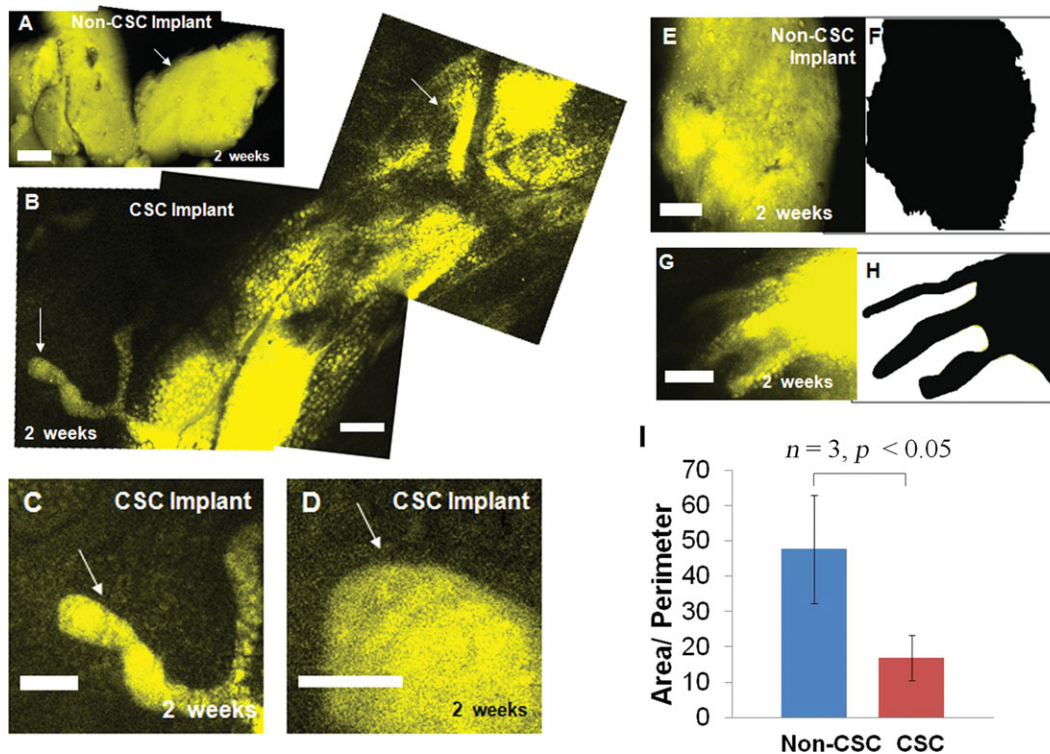


**Figure 6.** Transplantation of dye-labeled CSC from MMTV-Wnt1 mice results in rapid activation of invasive remodeling programs. (A): Mosaic, *in vivo* image of dye-labeled (yellow), 10,000 in non-CSC (non-Thy1<sup>+</sup> CD24<sup>+</sup>) cells in female, 3-month-old, nude mouse, 2 weeks after transplantation. The mosaic image is composed of projection images from a depth stack (see Materials and Methods). Cell mass appears yellow, and edges are quiescent at edge of transplant. Bar = 500  $\mu$ m. (B): Mosaic, *in vivo* image of dye-labeled (yellow), 10,000 CSC (Thy1<sup>+</sup> CD24<sup>+</sup>) cells in female, 3-month-old, nude mouse, 2 weeks after transplantation. Cell mass appears to be active with evidence of duct formation (arrow, bottom left) and evidence of invasiveness internally (arrow, top right). Bar = 500  $\mu$ m. (C): Single image from bottom left of (B), at a higher magnification, demonstrating evidence of ductal growth and branching. Bar = 100  $\mu$ m. (D): Same image as in (C) at higher magnification, focused on the structure appearing as a mammary bud in a newly forming duct with clear edges. Bar = 50  $\mu$ m. (E): *In vivo* image of dye-labeled, 10,000 non-CSC (non-Thy1<sup>+</sup> CD24<sup>+</sup>) cells in 3-month-old, nude mouse, 2 weeks after transplantation. Cell mass appears quiescent. Bar = 500  $\mu$ m. (F): The same image in (E) except outlined using Image J (see Materials and Methods). (G): *In vivo* image of dye-labeled, 10,000 CSC (Thy1<sup>+</sup> CD24<sup>+</sup>) cells in 3-month-old, nude mouse, 2 weeks after transplantation. Cell implant appears to have invasive portions. Bar = 500  $\mu$ m. (H): The same image in (G) except outlined using Image J (see Materials and Methods). (I): Bar graph demonstrating invasiveness as a function of area divided by perimeter. Images with more invasive features demonstrate a decreased ratio, as perimeter increases in proportion to area. This ratio was calculated in  $n = 3$  mice. TG condition displays increased invasiveness that is statistically significant ( $p < .005$ ). Abbreviation: CSC, cancer stem cell.

panel). However, when these cells were re-sorted, the cell population was not enriched, and only 20% of the cells from the initial sort repopulated the same gate (supporting information Fig. S10b left panel [top right gate] and right panel). Our data suggests that DB7 cells do not differentially express the Thy1 antigen and thus cannot be sorted using the MMTV-Wnt1 CSC and non-CSC phenotypes. Overall, our data strongly suggests that transplantation of CSC, but not non-CSC, results in a rapid and dynamic remodeling response of the endogenous mammary gland.

### Transplantation of Dye-Labeled CSC from MMTV-Wnt1 Mice Results in Rapid Activation of Invasive Remodeling Programs

CSC and non-CSC populations displayed differences in remodeling host, endogenous ducts after transplantation. Previous studies of CSC in the MMTV-Wnt1 model demonstrated that although both the CSC and non-CSC have some proliferative capacity, only the CSC grow continuously and form tumors. We hypothesized that invasive, MSC-specific remodeling programs may be shared by CSC. To this end, we dye-labeled CSC and non-CSC, transplanted them into adult nude mice, and imaged them 2 weeks later. To identify more imaging features of transplanted cells, we transplanted four

times more cells than in previous experiments (10,000 vs. 2,500). All non-CSC transplants appeared to have well demarcated, contiguous borders (Fig. 6A, arrow). In stark contrast, CSC transplants appeared to have more noncontiguous borders and overall more complex shapes (Fig. 6B, right, top arrow). Furthermore, CSC-transplanted cells displayed formation of duct-like structures (Fig. 6B left, bottom arrow). We observed these duct-like structures at higher magnifications too (Fig. 6C, 6D). These structures partially mimicked ductal growth and branching observed during development (compare Fig. 6B, 6C with Fig. 3C, 3D). Additional duct-like structures were present without branching (Fig. 6G, 6H). We observed a total of nine mammary duct-like structures in the CSC condition; four of which demonstrated branching and five of which were without branching. We observed only one in the non-CSC condition, and this did not have branching ( $n = 3$  transplants for both conditions). Because of this, we were not able to apply the branching analysis to compare growth of CSC and non-CSC. However, to quantify imaging features of the implants, we took advantage of the global imaging capability of our technique. We outlined the entire transplant (Fig. 6E–6H; supporting information Videos S9 [non-CSC], S10 [CSC]) and divided the area by the perimeter, for each mouse. The CSC fraction displayed a

significantly less ratio than the non-CSC fraction (Fig. 6I,  $n = 3$ ,  $p < .005$ ), indicating an increased perimeter in the CSC implants. Taken together, we conclude that dye-labeled CSC implants demonstrated more ductal growth, similar developing mammary gland, and demonstrate more “invasive”-like imaging features.

## DISCUSSION

Mammary gland remodeling is a central physiologic process, and pathological remodeling is associated with increased risk of tumor formation. While there has been an increased interest in tumor–stroma interactions, how tumors remodel the underlying endogenous mammary tree is poorly understood. To better understand the tumor cells’ effects on normal epithelium, we developed an approach to measure remodeling by *in vivo* imaging and analysis of the endogenous mammary tree. Using our imaging strategy, we demonstrated that the endogenous mammary ducts display TEB formation, side (lateral) budding and branching after CSC transplantation, consistent with endogenous remodeling. We also demonstrated that CSC themselves undergo rapid remodeling compared to non-CSC. Our novel approach, which is complementary to traditional techniques [9–12], combines cell sorting, cell transplantation, broad field-of-view *in vivo* imaging and quantification, fluorescent mice, and early time point analysis.

An important finding was that CSC from the MMTV-Wnt1 model can rapidly remodel endogenous ducts. The CSC remodeling response can be characterized by increased lateral branching and TEB formation. The changes in architecture are likely mediated by changes in MSC, or the MaCFC (immediate progenitor) population may be more active in the CSC compared with the non-CSC. Our *in vivo* mosaic images indicate that the endogenous remodeling response decreases with increasing distance from implantation, suggesting that a diffusible signal may participate in remodeling. Previously, transplanted fragments of MMTV-Wnt1 derived tumors into developing nude mice resulted in no remodeling of endogenous ducts, even when they were in direct contact. However, the authors transplanted hyperplastic fragments not cellular subsets of tumor [33]. Wnt expression has been associated with duct remodeling in the growing mammary duct [34] and might be involved in causing increasing remodeling in the case of MMTV-Wnt1 derived CSC. Future approaches to isolate and analyze small portions of tumor, and small neighboring portions of gland, to perform imaging at the single cell level, and to analyze single cells should lead to a more systematic understanding of the remodeling process. Nevertheless, our studies point toward the importance of *in vivo* imaging and differences in phenotype between cell lines and subpopulations of primary tumor cells. We speculate that mammary tree growth is constrained into a small number of growth “modules” such as global remodeling (regeneration), asymmetric duct formation (development), and lateral branching. We further speculate that tumor growth from CSC may be similarly constrained, and that comparisons of mammary tree growth and tumor growth may lead to new insights into tumor growth.

The DB7 cell transplantation studies demonstrated decreased duct signal, presumably from involution, apoptosis, necrosis, or assimilation into the primary tumor. Our efforts to analyze the DB7 cell line for Thy1<sup>+</sup>CD24<sup>+</sup> demonstrated that there is no distinguishable Thy1<sup>+</sup> population in the DB7 cells, so it is not clear whether the cell line has subpopulations of cells that behave differently. To our knowledge, a

CSC phenotype established through cell surface marker analysis followed by transplantation at limiting dilution has not been performed in the DB7 population. Another point that complicates comparison is the genetic basis of the DB7 oncogenesis due to PyMT antigen, which activates numerous cellular transcription factors, as compared to the expression of Wnt1, which is a secreted glycoprotein. Furthermore, adaptation to *in vitro* conditions is associated with changes to the cell which may not be present in primary tumor cells. Improvement of techniques in cell injection, manipulation of the mammary ducts, labeling, and imaging should assist in a continuing understanding of the differences between remodeling by primary tumors and the value of using cell lines in this setting.

Another important finding was that dye-labeled CSC themselves undergo remodeling, which, in some cases, are similar to the developing mammary tree. Studies using human breast tumors [17, 35] and mouse breast tumors [18] have demonstrated that CSC grow continuously but non-CSC have limited proliferative capacity. In the study by Liu et al. [35], bioluminescence imaging was used to demonstrate differences between CSC and non-CSC growth. However, individual, invasive events could not be captured, in part because bioluminescence has a much lower spatial resolution than IVM. Here, the use of IVM allowed visualization of several invasive events from CSC, in some cases ductal formation and branching (Fig. 3A–3D compared to Fig. 6B–6D). Since we did not see massive dye dilution of labeled cells during the CSC studies, we speculate that this may occur by a rapid, collective movement of cells, as is reported for *in vitro* mammary epithelial 3D cultures [36]. There is a possibility that nontransformed MSC contaminate our injections and can give rise to invasive ductal structures. However, we observed either microscopic and/or bulk tumors in all cases of CSC transplantation, which suggests that the invasive ductal structures are strongly associated with CSC activity but not non-CSC activity. Future work performing single cell clonal experiments, with improved ability to control injection location and imaging at higher spatial resolution, should help answer this question.

An important challenge in imaging the remodeling process was the quantitation of the highly localized phenomena, which we clearly observed after CSC transplantation. We observed that two of three parameters used to measure lateral branching only approached statistical significance ( $p < .056$ ). We feel the images themselves demonstrate increased lateral branching, and one reason statistical significance was not reached was because of our specific analysis approach. Rather than performing zooming to focus on observed local phenomena, we analyzed three standard sized images ( $2,297.92 \times 2,297.92 \mu\text{m}^2$  or approximately  $2.3 \times 2.3 \text{ mm}^2$ ). We took this approach despite the fact that side branching was highly localized, occurring on length scales of only 100–500  $\mu\text{m}$ . Thus, when we measured branching in each field of view, we were also including normal branching in our measurements, which would affect statistical significance when compared to analysis of normal ducts. Furthermore, by including three independent fields of view, we could also be introducing normal branching data into the analysis of the increased lateral branching that we observed. Future approaches will include more creative methods that are designed to analyze highly localized phenomena near transplanted CSC and non-CSC.

One strength of our approach is that with decreased cell numbers and with early time points, we visualized phenomena that had been previously unappreciated. Importantly, our imaging data suggest that MSC and CSC both have

invasive remodeling programs, but only CSC have lost tight control over these programs. However, our approach could identify these events but not determine a unique molecular signature for each event. Other than technical improvement of existing techniques, a critical challenge will be to better understand human CSC remodeling. For example, human CSC could be transplanted in “humanized” fat pads [37], which already contain regenerated, functional normal human mammary tree, in an immunocompromised mouse host. Then *in vivo* imaging of host, human ducts, could be used to assess and treat CSC-induced remodeling. Overall, our data points toward the potential of targeting CSC-specific remodeling and using *in vivo* imaging to understand the process.

### CONCLUSION

We have developed a novel approach to better understand how CSC interact with their microenvironment at macroscopic (whole tissue) and microscopic scales. Overall, our approach was to obtain serial *in vivo* images, or a graphic representation, of the complex remodeling process. We measured how CSC interact with the microenvironment by assessing how endogenous ducts are affected by CSC transplantation. Importantly, we demonstrate differences between CSC and non-CSC derived from MMTV-Wnt1 tumors. Examining endogenous ducts of CSC and non-CSC implanted mice, we show an increased number of short branches, branch points, ducts with greater than 40 branches, and histological evidence of increased branching. Examining CSC implants themselves,

we suggest that CSC implants invade into surrounding stroma with structures similar to developing mammary ducts (nine for CSC and one for non-CSC) and demonstrate overall changes in global morphology of transplants. Taken together, our data strongly suggest that CSC interacts uniquely with their microenvironment when compared to non-CSC, which could be used to develop approaches to therapeutically target CSC.

### ACKNOWLEDGMENTS

This work was supported in part by the NCI ICMIC P50CA114747 (S.S.G.), and Canary Foundation (S.S.G.). N.P. was supported in part by Stanford Dean’s Fellowship, and Stanford NIBIB T32 Training grant EB009035. The authors acknowledge Dr. Manish Patel for his assistance in lentiviral production, Dr. Robert Cho for experimental advice, Pauline Chu for her excellent assistance with preparation of histological slides, and Dr. Andrew Olson and the Stanford Neuroscience Microscopy Service (NIS) for assistance with the Two-Photon Microscope.

### DISCLOSURE OF POTENTIAL CONFLICTS OF INTEREST

The authors indicate no potential conflicts of interest.

### REFERENCES

- 1 Sternlicht MD, Kouros-Mehr H, Lu P et al. Hormonal and local control of mammary branching morphogenesis. *Differentiation* 2006;74:365–381.
- 2 Khokha R, Werb Z. Mammary gland reprogramming: Metalloproteinases couple form with function. *Cold Spring Harb Perspect Biol* 2011;3.
- 3 McCready J, Arendt LM, Rudnick JA et al. The contribution of dynamic stromal remodeling during mammary development to breast carcinogenesis. *Breast Cancer Res* 2010;12:205.
- 4 Radisky DC, Hartmann LC. Mammary involution and breast cancer risk: Transgenic models and clinical studies. *J Mammary Gland Biol Neoplasia* 2009;14:181–191.
- 5 O’Brien J, Schedin P. Macrophages in breast cancer: Do involution macrophages account for the poor prognosis of pregnancy-associated breast cancer? *J Mammary Gland Biol Neoplasia* 2009;14:145–157.
- 6 Wiseman BS, Werb Z. Stromal effects on mammary gland development and breast cancer. *Science* 2002;296:1046–1049.
- 7 Lanigan F, O’Connor D, Martin F et al. Molecular links between mammary gland development and breast cancer. *Cell Mol Life Sci* 2007;64:3159–3184.
- 8 Li Y, Hively WP, Varmus HE. Use of MMTV-Wnt-1 transgenic mice for studying the genetic basis of breast cancer. *Oncogene* 2000;19:1002–1009.
- 9 Blavier L, Lazaryev A, Dorey F et al. Matrix metalloproteinases play an active role in Wnt1-induced mammary tumorigenesis. *Cancer Res* 2006;66:2691–2699.
- 10 Kapoun AM, Shackelford GM. Preferential activation of Fgf8 by proviral insertion in mammary tumors of Wnt1 transgenic mice. *Oncogene* 1997;14:2985–2989.
- 11 Ettenberg SA, Charlat O, Daley MP et al. Inhibition of tumorigenesis driven by different Wnt proteins requires blockade of distinct ligand-binding regions by LRP6 antibodies. *Proc Natl Acad Sci USA* 2010;107:15473–15478.
- 12 Alexander CM, Reichsman F, Hinkes MT et al. Syndecan-1 is required for Wnt-1-induced mammary tumorigenesis in mice. *Nat Genet* 2000;25:329–332.
- 13 Stingl J, Eirew P, Ricketson I et al. Purification and unique properties of mammary epithelial stem cells. *Nature* 2006;439:993–997.
- 14 Shackleton M, Vaillant F, Simpson KJ et al. Generation of a functional mammary gland from a single stem cell. *Nature* 2006;439:84–88.
- 15 Tiede B, Kang Y. From milk to malignancy: The role of mammary stem cells in development, pregnancy and breast cancer. *Cell Res* 21:245–257.
- 16 Lobo NA, Shimono Y, Qian D et al. The biology of cancer stem cells. *Annu Rev Cell Dev Biol* 2007;23:675–699.
- 17 Al-Hajj M, Wicha MS, Benito-Hernandez A et al. Prospective identification of tumorigenic breast cancer cells. *Proc Natl Acad Sci USA* 2003;100:3983–3988.
- 18 Cho RW, Wang X, Diehn M et al. Isolation and molecular characterization of cancer stem cells in MMTV-Wnt-1 murine breast tumors. *Stem Cells* 2008;26:364–371.
- 19 Vaillant F, Asselin-Labat ML, Shackleton M et al. The mammary progenitor marker CD61/beta3 integrin identifies cancer stem cells in mouse models of mammary tumorigenesis. *Cancer Res* 2008;68:7711–7717.
- 20 Diehn M, Cho RW, Lobo NA et al. Association of reactive oxygen species levels and radioresistance in cancer stem cells. *Nature* 2009;458:780–783.
- 21 Clarke MF. What can we learn about breast cancer from stem cells? *Adv Exp Med Biol* 2008;617:17–22.
- 22 Shimono Y, Zabala M, Cho RW et al. Downregulation of miRNA-200c links breast cancer stem cells with normal stem cells. *Cell* 2009;138:592–603.
- 23 Tilli MT, Parrish AR, Cotalra I et al. Comparison of mouse mammary gland imaging techniques and applications: Reflectance confocal microscopy, Gfp imaging, and ultrasound. *BMC Cancer* 2008;8:21.
- 24 Yang M, Li L, Jiang P et al. Dual-color fluorescence imaging distinguishes tumor cells from induced host angiogenic vessels and stromal cells. *Proc Natl Acad Sci USA* 2003;100:14259–14262.
- 25 Ahmed F, Wyckoff J, Lin EY et al. GFP expression in the mammary gland for imaging of mammary tumor cells in transgenic mice. *Cancer Res* 2002;62:7166–7169.
- 26 Jansen SA, Conzen SD, Fan X et al. Detection of in situ mammary cancer in a transgenic mouse model: In vitro and in vivo MRI studies demonstrate histopathologic correlation. *Phys Med Biol* 2008;53:5481–5493.
- 27 Creamer BA, Triplett AA, Wagner KU. Longitudinal analysis of mammary tumorigenesis using a novel tetracycline-inducible mouse model and in vivo imaging. *Genesis* 2009;47:234–245.
- 28 Liu H, Patel MR, Prescher JA et al. Cancer stem cells from human breast tumors are involved in spontaneous metastases in orthotopic mouse models. *Proc Natl Acad Sci USA* 107:18115–18120.

- 29 Okabe M, Ikawa M, Kominami K et al. 'Green mice' as a source of ubiquitous green cells. *FEBS Lett* 1997;407:313–319.
- 30 Deome KB, Faulkin LJ, Jr., Bern HA et al. Development of mammary tumors from hyperplastic alveolar nodules transplanted into gland-free mammary fat pads of female C3H mice. *Cancer Res* 1959;19:515–520.
- 31 Webster MA, Hutchinson JN, Rauh MJ et al. Requirement for both Shc and phosphatidylinositol 3' kinase signaling pathways in polyomavirus middle T-mediated mammary tumorigenesis. *Mol Cell Biol* 1998;18:2344–2359.
- 32 Borowsky AD, Namba R, Young LJ et al. Syngeneic mouse mammary carcinoma cell lines: Two closely related cell lines with divergent metastatic behavior. *Clin Exp Metastasis* 2005;22:47–59.
- 33 Lin TP, Guzman RC, Osborn RC et al. Role of endocrine, autocrine, and paracrine interactions in the development of mammary hyperplasia in Wnt-1 transgenic mice. *Cancer Res* 1992;52:4413–4419.
- 34 Bradbury JM, Edwards PA, Niemeyer CC et al. Wnt-4 expression induces a pregnancy-like growth pattern in reconstituted mammary glands in virgin mice. *Dev Biol* 1995;170:553–563.
- 35 Liu H, Patel MR, Prescher JA et al. Cancer stem cells from human breast tumors are involved in spontaneous metastases in orthotopic mouse models. *Proc Natl Acad Sci USA* 2010;107:18115–18120.
- 36 Ewald AJ, Brenot A, Duong M et al. Collective epithelial migration and cell rearrangements drive mammary branching morphogenesis. *Dev Cell* 2008;14:570–581.
- 37 Kuperwasser C, Chavarria T, Wu M et al. Reconstruction of functionally normal and malignant human breast tissues in mice. *Proc Natl Acad Sci USA* 2004;101:4966–4971.



See [www.StemCells.com](http://www.StemCells.com) for supporting information available online.